The Astrophysical Journal, 934:49 (14pp), 2022 July 20 https://doi.org/10.3847/1538-4357/ac7805

A Candle in the Wind: A Radio Filament in the Core of the A3562 Galaxy Cluster

S. Giacintucci[1], T. Venturi[2], M. Markevitch[3], H. Bourdin[4,5], P. Mazzotta[4,5], P. Merluzzi[6], D. Dallacasa[2,7], S. Bardelli[8], S. P. Sikhosana[9,10], O. Smirnov[11,12], and G. Bernardi[2,12,13]
[1] Naval Research Laboratory, 4555 Overlook Avenue SW, Code 7213, Washington, DC 20375, USA; simona.giacintucci@nrl.navy.mil
[2] INAF—Istituto di Radioastronomia, via Gobetti 101, I-40129 Bologna, Italy
[3] NASA/Goddard Space Flight Center, Greenbelt, MD 20771, USA
[4] Università di Roma Tor Vergata, Via della Ricerca Scientifica, I-00133 Roma, Italy
[5] INFN, Sezione di Roma 2, Università di Roma Tor Vergata, Via della Ricerca Scientifica, 1, Roma, Italy
[6] INAF—Osservatorio Astronomico di Capodimonte, Salita Moiariello 16, I80131 Napoli, Italy
[7] Dipartimento di Fisica e Astronomia, Università di Bologna, Via Gobetti 93/2, I-40129 Bologna, Italy
[8] INAF—Osservatorio di Astrofisica e Scienza dello Spazio di Bologna—via Gobetti 93/3, I-40129 Bologna, Italy
[9] Astrophysics Research Centre, University of KwaZulu-Natal, Durban 4041, South Africa
[10] School of Mathematics, Statistics, and Computer Science, University of KwaZulu-Natal, Westville 3696, South Africa
[11] NRAO, PO Box 0, Socorro, NM 87801, USA
[12] Department of Physics and Electronics, Rhodes University, PO Box 94, Makhanda 6140, South Africa
[13] South African Radio Astronomy Observatory, 2 Fir Street, Black River Park, Observatory, Cape Town 7925, South Africa
Received 2022 March 1; revised 2022 June 8; accepted 2022 June 11; published 2022 July 25

Abstract

Using a MeerKAT observation of the galaxy cluster A3562 (a member of the Shapley supercluster), we have discovered a narrow, long and straight, very faint radio filament, which branches out at a straight angle from the tail of a radio galaxy located in projection near the core of the cluster. The radio filament spans 200 kpc and aligns with a sloshing cold front seen in the X-rays, staying inside the front in projection. The radio spectral index along the filament appears uniform (within large uncertainties) at $\alpha \simeq -1.5$. We propose that the radio galaxy is located outside the cold front but dips its tail under the front. The tangential wind that blows there may stretch the radio plasma from the radio galaxy into a filamentary structure. Some reacceleration is needed in this scenario to keep the radio spectrum uniform. Alternatively, the cosmic-ray electrons from that spot in the tail can spread along the cluster magnetic field lines, straightened by that same tangential flow, via anomalously fast diffusion. Our radio filament can provide constraints on this process. We also uncover a compact radio source at the brightest cluster galaxy that is 2–3 orders of magnitude less luminous than those in typical cluster central galaxies—probably an example of a brightest cluster galaxy starved of accretion fuel by gas sloshing.

Unified Astronomy Thesaurus concepts: Galaxy clusters (584); Radio galaxies (1343); Intracluster medium (858); Tailed radio galaxies (1682); Radio continuum emission (1340); Extragalactic radio sources (508)

1. Introduction

The current generation of sensitive, high-resolution radio interferometers, such as the LOw Frequency ARray (LOFAR; van Haarlem et al. 2013), upgraded Giant Metrewave Radio Telescope (uGMRT; Gupta et al. 2017), Jansky Very Large Array (Perley et al. 2011) and the Square Kilometer Array (SKA) precursors Australia SKA Pathfinder (ASKAP; Hotan et al. 2021) and MeerKAT (Jonas & MeerKAT Team 2016; Camilo et al. 2018) have started revealing new phenomena that have been hiding under the sensitivity and resolution limits of earlier instruments. Of particular interest are the strikingly long and narrow, very faint synchrotron filaments that MeerKAT observations have discovered in unexpected places such as in the Galactic center (Heywood et al. 2019, 2022), between the lobes of the radio galaxy ESO 137–006 in the Norma galaxy cluster (Ramatsoku et al. 2020), emerging from the radio jets of the radio galaxy IC 4296 in A3565 (Condon et al. 2021), departing from the northern lobe of the radio galaxy 3C 40B, and between 3C 40B and the nearby radio galaxy 3C 40A in A194 (Knowles et al. 2022).

Radio filamentary structures have been seen before, for instance, those embedded within the lobes and tails of radio galaxies (see Hardcastle et al. 2019; Maccagni et al. 2020; Brienza et al. 2021; Gendron-Marsolais et al. 2021, for recent examples) and in cluster radio relics (e.g., Slee et al. 2001; Owen et al. 2014; Di Gennaro et al. 2018a; Rajpurohit et al. 2020; Knowles et al. 2022). MeerKAT now reveals low surface brightness radio filaments extending outside the radio lobes and tails. In fact, the most prominent radio filament in ESO 137–006 is a 80 kpc long, collimated and straight thread that connects the two opposing radio lobes, bypassing the central nucleus (Ramatsoku et al. 2020).

Radio filamentary features extending from, or in the vicinity of, a radio galaxy have also been found with the VLA (e.g., in 3C 129, A2256, and the Perseus cluster; Lane et al. 2002; Owen et al. 2014; Gendron-Marsolais et al. 2020, 2021) and with LOFAR and GMRT (e.g., Shimwell et al. 2016; de Gasperin et al. 2017; Clarke et al. 2019; Botteon et al. 2020a, 2021; Brienza et al. 2022; Pandge et al. 2022) at low radio frequencies, which are sensitive to the radio emission arising from old cosmic-ray electrons.

The nature of these synchrotron threads is unclear. For the MeerKAT radio filament between the ESO 137–006 lobes, Ramatsoku et al. (2020) suggested "some sort of reconnection" in the cluster magnetic field around the two radio lobes, possibly caused by its interaction with the lobes themselves.

Table 1
MeerKAT Images

ν (MHz)	$\Delta\nu$ (MHz)	FWHM (arcsec × arcsec)	rms (μJy beam^{-1})
1284	856	$6\farcs4 \times 6\farcs0$	6
1284	856	$15''$	9
1070	428	$9\farcs4 \times 8\farcs6$	10
1498	428	$7\farcs4 \times 6\farcs7$	8
1498	428	$9\farcs4 \times 8\farcs6$	8
1070	428	$15''$	14
1498	428	$15''$	10
1070	428	$30''$	40
1498	428	$30''$	25

Note. Column (1): central frequency. Column (2): bandwidth. Column (3): FWHM of the radio beam. Column (4): rms noise level (1σ). All images were made using a Briggs robust parameter of 0.

While the polarization properties of the ESO 137–006 threads are still unknown, the radio filaments in IC 4296 (Condon et al. 2021) were found to be highly polarized with an ordered longitudinal configuration of the magnetic field vectors, suggesting coherent magnetic field structures along their entire length (∼50 kpc). Condon et al. (2021) proposed that these faint synchrotron threads are created by relativistic electrons escaping from helical Kelvin–Helmholtz instabilities in the radio jets and suggested that their structure traces the magnetic field lines that are frozen into the ambient gas of the host galaxy. Knowles et al. (2022) speculated that the radio filaments linked to the radio galaxies in A194 may illuminate magnetic flux tubes in the intracluster medium (ICM; e.g., Parrish et al. 2012; Birkinshaw & Worrall 2015; Donnert et al. 2018). The synchrotron emission is proportional to $N_e B^2$, where N_e is the density of the relativistic electrons and B is the magnetic field strength; therefore, it is natural to expect that such radio filaments map the structure of the underlying magnetic fields. However, a peculiar distribution of N_e may also result in filamentary structures. Numerical simulations have shown, in fact, that ICM "weather" flows can advect the cosmic-ray electrons from active galactic nucleus (AGN) radio lobes and create filamentary patterns (Vazza et al. 2021; ZuHone et al. 2021). The structures seen by LOFAR at low radio frequencies may indeed trace the spatial distribution of aged cosmic rays and the various acceleration mechanisms in the ICM (Brunetti & Jones 2014; van Weeren et al. 2019). These low-brightness radio phenomena are opening a new window onto the physical processes occurring in the hot magnetized ICM, which is the final repository for the cosmic rays ever produced by AGNs and cosmological shocks.

Another interesting example of this new phenomenon has recently been discovered by MeerKAT in A3562 (Venturi et al. 2022, hereafter V22), in the core of the Shapley MeerKAT reveals a faint radio thread branching out from the tail of the head–tail radio galaxy J1333–3141 and spanning a large length of ∼200 kpc. As we will show below, the thread appears to be connected to the structure of the cluster thermal gas. We believe that this specimen can illuminate the nature and origin of this new phenomenon and potentially provide constraints on the ICM physics.

In this paper, we present an imaging and spectral analysis of this radio filament using the new MeerKAT data and complement it with a reanalysis of the archival X-ray Chandra and XMM-Newton observations. We also study the faint radio emission associated with the brightest cluster galaxy (BCG) and its connection to the properties of the surrounding thermal gas.

We use a ΛCDM cosmology with $H_0 = 70\,\mathrm{km\,s^{-1}\,Mpc^{-1}}$, $\Omega_m = 0.3$, and $\Omega_\Lambda = 0.7$. At the redshift of A3562 ($z = 0.049$) $1''$ corresponds to ∼1 kpc. All errors are quoted at the 68% confidence level. The radio spectral index α is defined according to $S_\nu \propto \nu^\alpha$, where S_ν is the flux density at the frequency ν.

2. MeerKAT Observations

The cluster A3562 (R.A.$_{J2000} = 13^h\ 33^m\ 47^s$, decl.$_{J2000} = -31°\ 40'\ 37''$) was observed by MeerKAT on 2019 July 7 (AO1, proposal ID SCI-20190418-OS-01) for a total of 10 hr on source, with 64 antennas, a total observing bandwidth of 856 MHz, and a central frequency of 1284 MHz. In V22, this observation was complemented with observations centered on the nearby SC 1329–313 group and on the cluster A3558, taken as part of the MeerKAT Galaxy Cluster Legacy Survey (GCLS; Knowles et al. 2022) and MeerKAT scientific commissioning, to obtain a mosaic encompassing the whole A3558 complex in the Shapley core. The mosaic is presented in V22 along with an ASKAP 887 MHz image of the same region and a morphological and spectral study of the extended radio sources in the whole complex. In this paper, we focus on the region of A3562, the easternmost cluster in the A3558-complex chain.

We use the MeerKAT proprietary observations and refer to V22 for a description of the data calibration. We obtained images at 1284 MHz from the full-band data set (0.9–1.7 GHz) with $6''$ and $15''$ resolution. We also obtained pairs of sub-band images, centered at 1070 and 1498 MHz, at three different resolutions to measure the in-band spectral indices and image the spectral index distribution. A summary of these images is given in Table 1. All images were produced as described in V22 using wsclean (Offringa et al. 2014; Offringa & Smirnov 2017) with a Briggs robust parameter of 0 (Briggs 1995) and fitting a fourth-order polynomial to account for wide-band spectral effects. No correction for the MeerKAT primary-beam attenuation was applied to the images, as our analysis is limited to a region within $8'$ from the phase center, where the effect is negligible (Mauch et al. 2020). The average residual amplitude calibration errors are estimated to be of the order of 5% (V22).

3. MeerKAT View of A3562

In Figure 1(a), we show the full-band (0.9–1.7 GHz) image of A3562 with $6''$ resolution from the proprietary data. In Figure 1(b), we show an image of the same region convolved with a $15''$ circular beam. The images have a sensitivity of 6 and 9 μJy beam^{-1}, which is almost an order-of-magnitude increase in sensitivity over previous best radio observations of A3562 (Venturi et al. 2003; Giacintucci et al. 2005, hereafter V03 and G05, respectively).

The head–tail radio source J1333–3141 and surrounding diffuse radio halo were known before (V03; G05; Venturi et al. 2000; Di Gennaro et al. 2018b). The head–tail source is located $\sim 1' = 60$ kpc (projected) away from BCG and is associated with a cluster member galaxy with a radial velocity $cz = 15{,}068$ km s^{-1} that is only ∼283 km s^{-1} (about one-third of the velocity dispersion, $\sigma = 769 \pm 30$ km s^{-1}) from the cluster mean velocity ($cz = 14{,}786$ km s^{-1}; Haines et al. 2018).

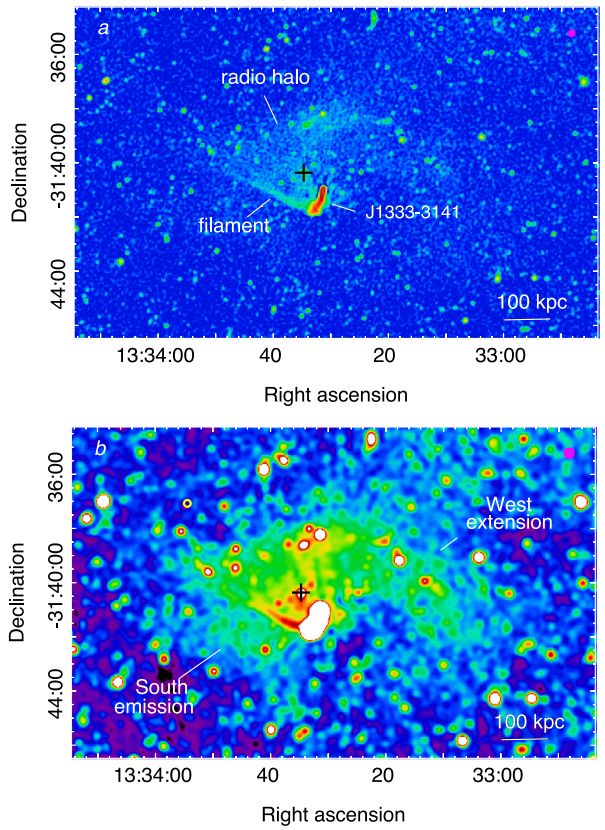

Figure 1. MeerKAT 1284 MHz images with an angular resolution of $6''.4 \times 6''.0$, in position angle (a) 146° and (b) 15°. The beam size (FWHM) is shown by a magenta circle in the upper right corner of each panel. The rms noise is $1\sigma = 6$ μJy beam^{-1} and $1\sigma = 9$ μJy beam^{-1}, respectively. The black plus sign marks the position of the BCG.

The improved sensitivity and angular resolution of the new MeerKAT image reveal new details and previously unknown features in A3562, which we describe in the next sections.

3.1. The Radio Filament

The most striking new feature is the faint, straight radio filament that follows the southern edge of the bright region of the radio halo in the cluster core. The radio filament appears to branch out at about a right angle from the J1333–3141 tail and can be traced for approximately 200 kpc eastward (see the zoomed-in images in Figure 2). It is narrow (∼8−10 kpc) and shows a possible fork at ∼60 kpc from the tail, where it seems to split into two fainter threads. One of them continues roughly along the original direction, whereas the other seems to depart at an angle of ∼15° from the original axis, merging (in projection) into the halo emission. The radio filament is also visible in the ASKAP image at 887 MHz (13″ resolution, V22), but with slightly lower signal-to-noise ratio due to the sensitivity of the ASKAP observation (∼30 μJy beam^{-1} local noise).

3.2. The Radio Halo

Images of the radio halo at 1.4 GHz (VLA) and at lower frequencies (GMRT) were presented in V03 and G05, where diffuse emission was detected up to a largest scale of 500 kpc along the east–west direction. In the new, high-sensitivity MeerKAT images (Figure 1), the halo appears fairly more extended southward (south emission) and westward (west extension), reaching ∼650 kpc in east–west direction.

The south emission is a new feature. It is a 300×150 kpc^2 region, just south of the newly discovered radio filament, with an average surface brightness of ∼0.2 μJy arcsec^{-1} (the average brightness in the halo is ∼0.5 μJy arcsec^{-1}).

To the west, the halo shows an extension that can be traced for ∼300 kpc. This feature had been partially seen in previous images (e.g., filament in Figure 9 in G05). It appears to point toward the neighboring group SC 1329–313, believed to have recently interacted with A3562 (Finoguenov et al. 2004, hereafter F04; G05). Patches of diffuse emission in the region between A3562 and SC 1329–313 were found in previous images (G05), suggesting a possible radio bridge between the cluster and nearby group. The existence of this bridge was clearly confirmed by the MeerKAT images presented in V22 (which we also report in Figure 12 in the Appendix), where a 800 kpc long structure connects the radio halo to SC 1329–313. Along with confirming the radio bridge, the V22 MeerKAT mosaic also unveiled a striking, megaparsec-scale arc of radio emission linking both objects from the north (see also Figure 12). Both the bridge and arc have a very low surface brightness of ∼0.1 μJy arcsec^{-1} and represent a unique detection of intracluster emission at GHz frequencies, only possible thanks to the exquisite *uv* coverage and sensitivity of MeerKAT. Detections of intracluster bridges have been reported at much lower frequencies in the Coma Cluster (Kim et al. 1989; Venturi et al. 1990; Brown & Rudnick 2011; Bonafede et al. 2021) and recently in the cluster pairs A399–A401 (Govoni et al. 2019) and A1758N–A1758S (Botteon et al. 2020b) with LOFAR at 144 MHz.

An updated radio spectrum of the halo, combining old (V03, G05) and new (MeerKAT, ASKAP) flux density measurements, has been presented in V22. Its steep spectral slope of $\alpha = -1.5 \pm 0.2$ between 332 and 1284 MHz places the A3562 halo in the class of ultra−steep-spectrum radio halos (e.g., Brunetti et al. 2008). Because of its relatively compact extent and low radio luminosity ($P_{1.4\,\mathrm{GHz}} \sim 1.1 \times 10^{23}$ W Hz^{-1}; V03), this halo is also one of the smallest and least powerful among the cluster radio halo population (e.g., van Weeren et al. 2019).

3.3. The BCG Emission

Another feature unveiled by the MeerKAT image of A3562 is weak radio emission at the position of the BCG. In Figure 3, we show the 1284 MHz radio contours overlaid on the VLT Survey Telescope (VST) OmegaCAM *g*-band image of the galaxy from the Shapley Supercluster Survey (ShaSS; Merluzzi et al. 2015). The radio emission consists of a compact component with 0.47 ± 0.02 mJy flux and coincident with the optical peak and an additional structure extending ∼10 kpc southward and with a flux of 0.31 ± 0.02 mJy. The total radio flux is 0.78 ± 0.04 mJy, and the luminosity at 1284 MHz is 4×10^{21} W Hz^{-1}.

The source was also detected in the ASKAP image at 887 MHz (V22) and by the VLA at 1400 MHz (Miller 2005) with unresolved morphology at a resolution of 13″ and 16″. A very faint compact source is also visible in the existing GMRT images at lower frequencies (G05; Di Gennaro et al. 2018b). No radio source is detected by the Australia Telescope Compact Array at 2360 MHz (Venturi et al. 2000), by the

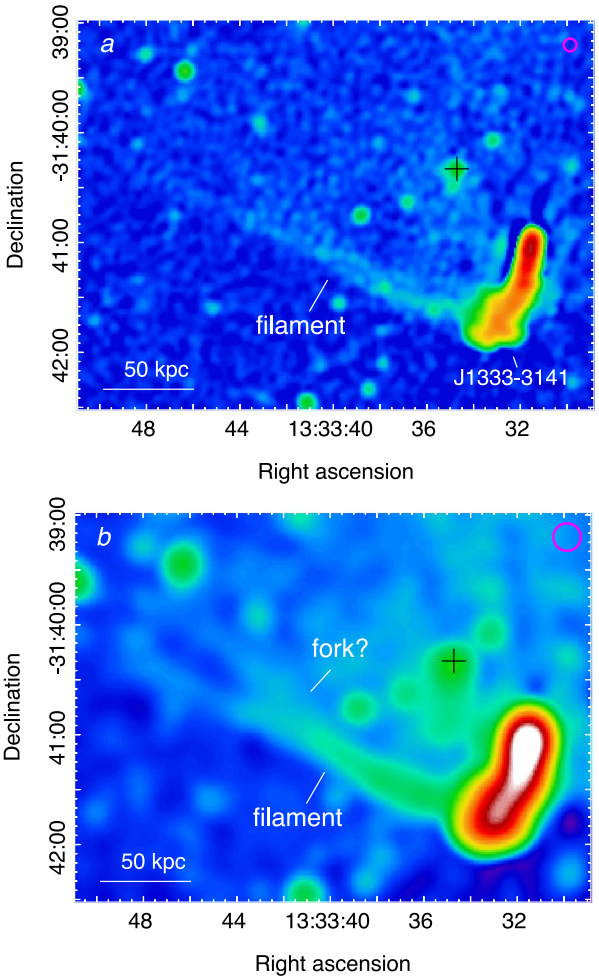

Figure 2. MeerKAT 1284 MHz images (same as in Figure 1) of the radio filament that starts from the end of the tail of J1333–3141 and extends ∼200 kpc eastward. A possible fork is seen at ∼60 kpc from the tail. The beam size is shown by a magenta circle in the upper right corner of each panel. The black plus sign marks the position of the BCG.

VLA at 4860 and 8460 MHz (V03), and in the Quick Look images at 3000 MHz from epochs 1.2 and 2.1 of the VLA Sky Survey (VLASS; Lacy et al. 2020).

In Table 2, we summarize the BCG total flux density and 3σ upper limits at all frequencies.[19] For MeerKAT, we report the flux density measured on the full-band image at 1284 MHz (Figure 3) and on the two high-resolution sub-band images at 1070 and 1498 MHz (Table 1). Flux density errors include local noise level and residual amplitude uncertainties, as reported in the references.

As visible in Figure 3, the radio emission is associated with the nucleus of the galaxy and is entirely embedded within the optical halo, which is very extended (∼180 kpc) and asymmetrical in the east–west direction. The white arrows mark the location of sharp, shell-like edges (or ripples; e.g., Schweizer & Seitzer 1988; Buta 2013) in the outer regions of the galaxy (see also Di Gennaro et al. 2018b). These kinds of

[19] A negative artifact affects the BCG location on the GMRT image at 327 MHz; therefore, we were not able to measure a reliable flux at this frequency.

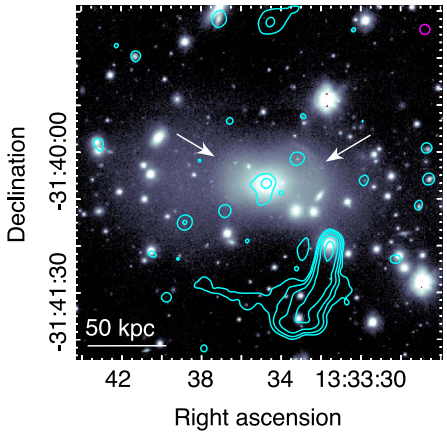

Figure 3. MeerKAT 0.9–1.7 GHz contours (from Figure 1(a)) overlaid on the VST-OmegaCAM g-band image of the BCG. Contours start at 50 μJy beam^{-1} and then scale by a factor of 4. The radio beam size is shown by the magenta circle. Arrows mark shell-like edges (or ripples) in the outer regions of the galaxy (see also di Gennaro et al. 2018b).

Table 2
BCG Radio Flux Densities

Frequency (MHz)	Flux Density (mJy)	Reference
235	4.7 ± 1.5	G05
610	1.4 ± 0.3	G05
887	1.22 ± 0.07	V22
1070	0.93 ± 0.05	This work
1284	0.78 ± 0.04	This work
1498	0.62 ± 0.03	This work
1400	0.51 ± 0.09	Miller (2005)
2360	<0.5	Venturi et al. (2000)
3000	<0.4	VLASS (Lacy et al. 2020)
4860	<0.2	V03
8460	<0.1	V03

Notes. Flux density errors include local noise level and residual amplitude uncertainties, as reported in the references.

structures are believed to be late-stage remnants of a merger between a large elliptical and a smaller companion disk galaxy (e.g., Quinn 1984).

4. Radio Spectral Analysis

G05 examined the distribution of the spectral index over the radio halo region using a 332–1400 MHz spectral index map with a relatively coarse resolution of ∼40″. Here we use the sensitivity and higher resolution of the new MeerKAT data to study the spectral index distribution in greater spatial detail.

4.1. Spectral Index Images

We computed a MeerKAT in-band spectral index map by comparing a pair of images centered at 1070 and 1498 MHz, convolved with a 15″ circular beam (Table 1). The spectral index was calculated in each pixel where both images have a signal above the 5σ level. The resulting spectral index map is shown in colors in Figure 4 (top), with 5σ contours from Figure 1(b) overlaid in white. The bottom panel shows the corresponding spectral index uncertainty map, in which the main contribution

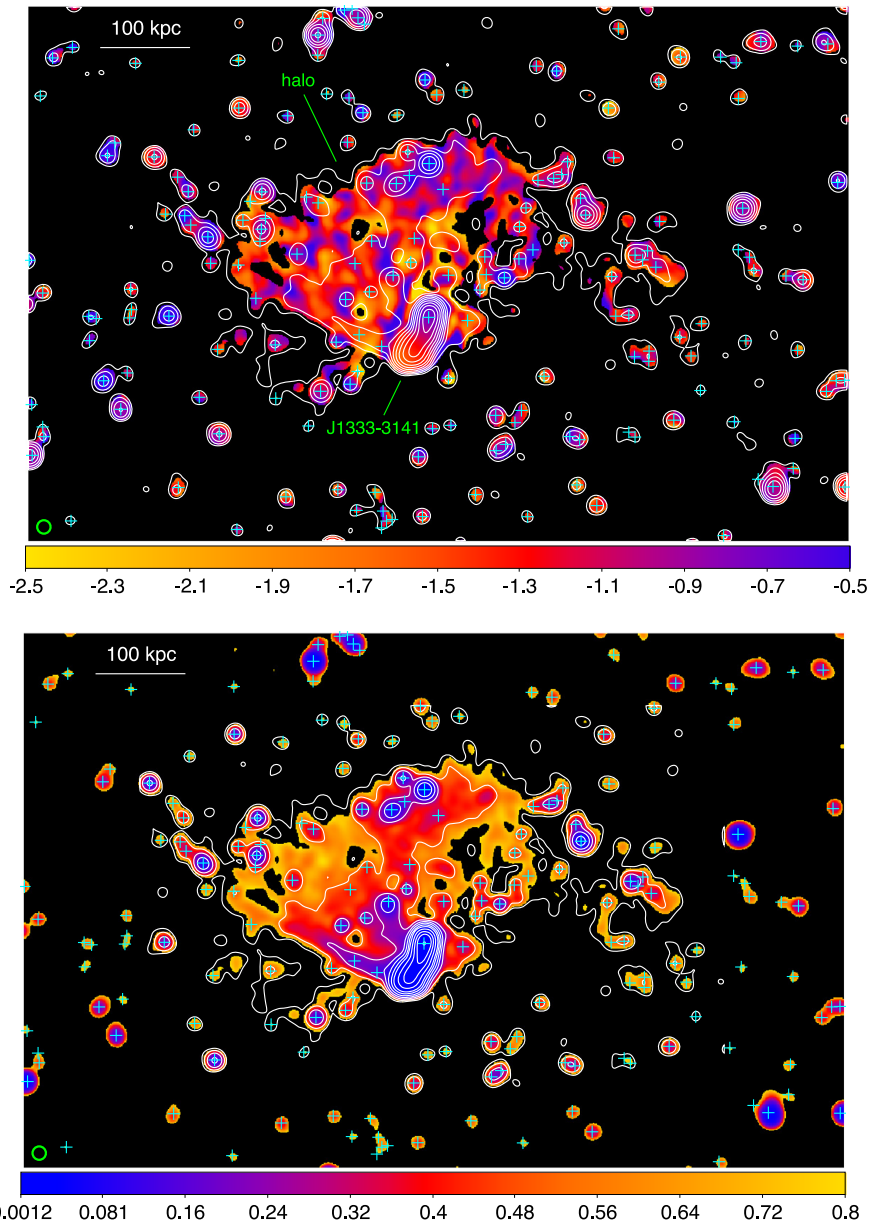

Figure 4. Color-scale images of the MeerKAT in-band (1070–1498 MHz) spectral index distribution in the head–tail source J1333–3141 and radio halo at a resolution of 15″ (top) and corresponding uncertainty map (bottom). Color bars are the spectral index (top) and spectral index error (bottom). In both panels, the contours from the full-band image at matching resolution (Figure 1(b)) are overlaid on the color map. Contours start at $5\sigma = 45$ μJy beam^{-1} and scale by a factor of 2. Cyan plus signs mark the position of the discrete radio sources identified by the PyBDSF source finding on the full-band, high-resolution image (Figure 1(a)). The beam size is shown by the green circle in the lower left corner of each panel.

comes from the proximity of the frequencies. Cyan plus signs mark the position of discrete radio sources that were identified using the full-band, high-resolution image (Figure 1(a)) and the Python Blob Detection and Source Finder software (PyBDSF; Mohan & Rafferty 2015). Following the same procedure, we obtained a low-resolution (30″) in-band spectral index map using a 3σ brightness cutoff in the individual 1070 and 1498 MHz images (Table 1). The spectral index image is shown in the top panel of Figure 5, and the associated uncertainty image is shown in the bottom panel. Superposed are the 3σ contours from the full-band image at matching resolution.

Along the 80 kpc long head–tail source J1333–3141 in Figure 4, we observe a clear gradual steepening from $\alpha \sim -0.6$ (head) to -1.5 (end of the tail; see also Section 4.2 and Figure 6). A similar trend was also seen in the spectral index maps in G05. Artifacts due to residual image errors around J1333–3141 cause the spectral index values to be unreliable in the immediate surrounding of this source, in particular in a very steep spectrum region (yellow) around the head and in a pair of low-α *bars* (dark blue) parallel to the tail in Figure 4. Unfortunately, one of these bars affects the location where the radio filament branches out

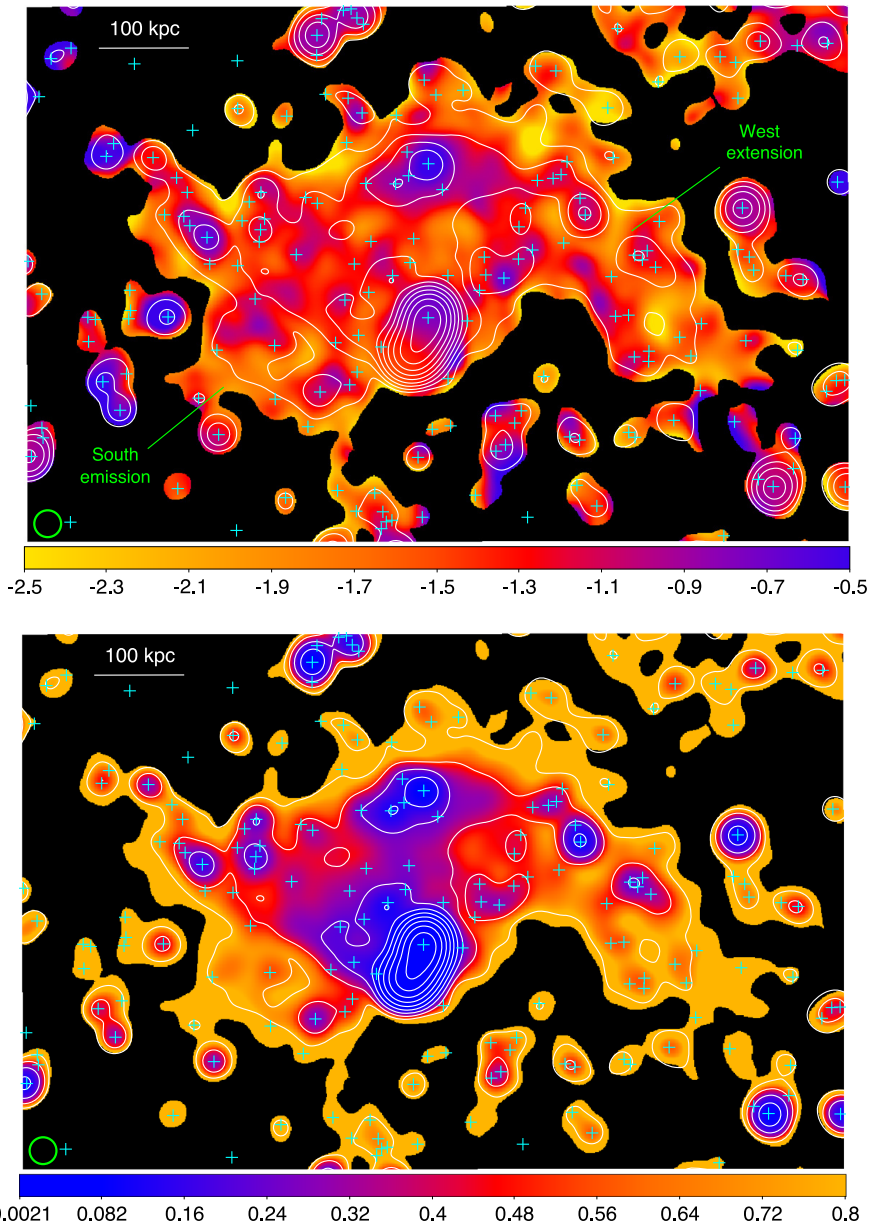

Figure 5. Color-scale images of the MeerKAT in-band (1070–1498 MHz) spectral index image at a resolution of 30″ (top) and corresponding uncertainty map (bottom). Color bars are the spectral index (top) and spectral index error (bottom). In both panels, the contours from the full-band image at matching resolution are overlaid on the color map. Contours start at $5\sigma = 75$ μJy beam^{-1} and scale by a factor of 2. Cyan plus signs mark the position of the discrete radio sources identified by the PyBDSF source finding on the full-band, high-resolution image (Figure 1(a)). The beam size is shown by the green circle in the lower left corner of each panel.

from the tail of J1333–3141. Beyond this region, the spectral index of the filament appears relatively constant along its whole 200 kpc length, with an average of -1.5. This value is similar to the spectral index in the terminal region of the head–tail source, from where the radio filament emerges. In Section 4.2, we examine in detail the spectral behavior along J1333–3141 and the filament.

In the halo region, an average value of $\alpha \sim -1.5$ is observed across most of the halo, including the west extension and newly detected south emission, in agreement with the G05 map and with the integrated spectrum of the halo in V22. The apparent structure in the spectral index maps within the halo on $\lesssim 1'$ scales (Figures 4 and 5) is not statistically significant. We searched for variations by deriving spectral index values for a grid of $40'' \times 40''$ beam-independent regions, as well as for several larger ($\sim$4–8 arcmin^2) regions, masking the head–tail source, filament, and discrete radio sources. All values were consistent with the average within statistical uncertainties, which are large owing to the limited frequency coverage. Upcoming uGMRT observations at lower frequencies, in combination with the MeerKAT data presented here, will provide better sensitivity to spatial variations of the halo spectral index.

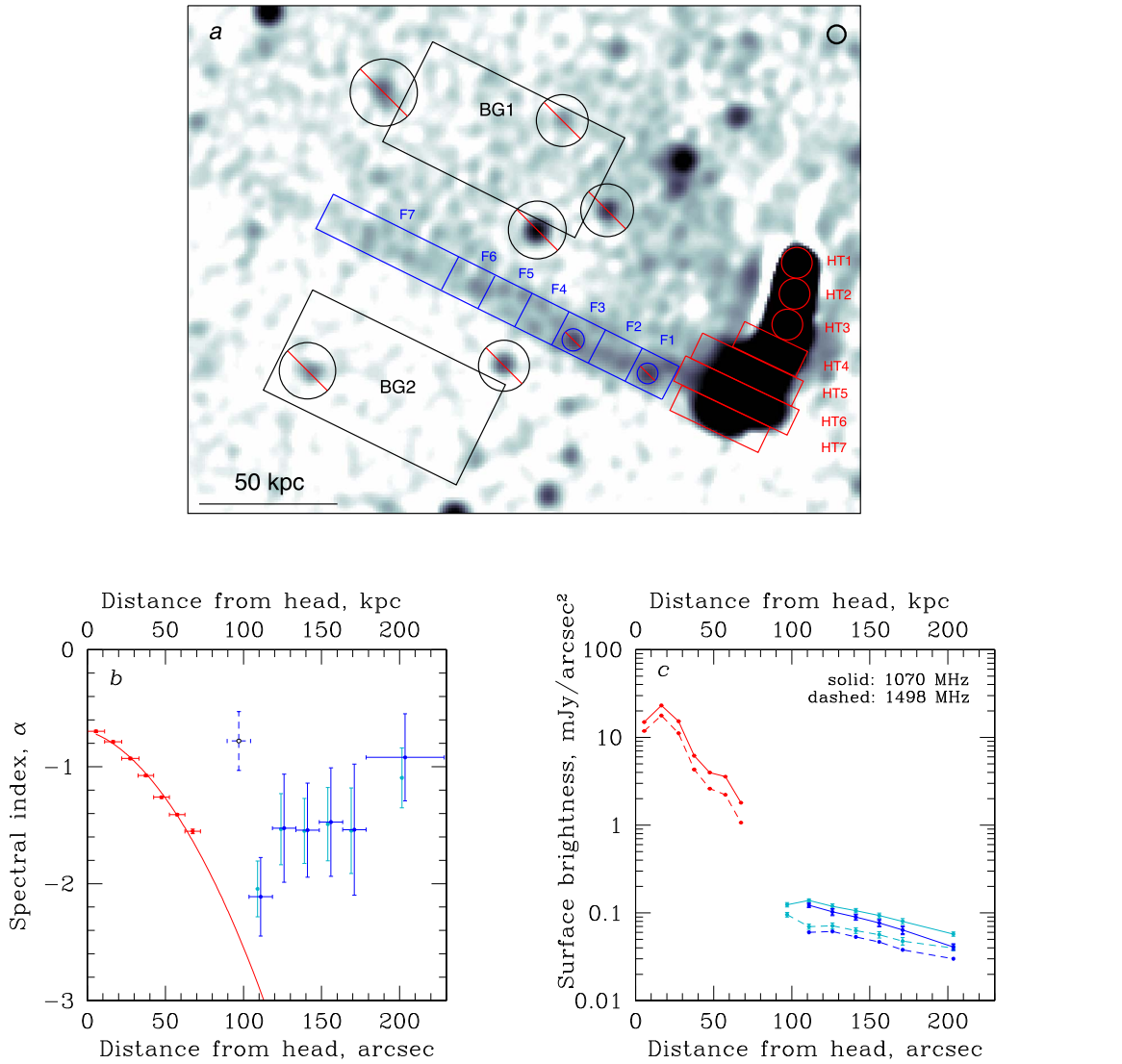

Figure 6. MeerKAT 1070–1498 MHz spectral index profiles (panel (b)) and surface brightness profiles (panel (c)) at 1070 MHz (solid lines) and 1498 MHz (dashed lines) along the head–tail source (red) and radio filament (cyan and blue). The profiles were computed using the regions shown in panel (a) and overlaid on the full-band image at 1284 MHz. The beam size is shown in black in the upper right corner of the image. Discrete sources in the F1–F7, BG1, and BG2 regions were masked out. The region F1 (shown with dashes in panel (b)) is affected by residual image artifacts near the bright head–tail emission. The filament data points (except F1) have been corrected for the background halo emission, estimated using the BG1 and BG2 regions (see text). Uncorrected data points are shown in cyan; corrected points are shown in blue. The head–tail spectral index profile is well fitted by a JP model (solid red line), as described in the text.

4.2. Spectral Index Profiles

We extracted a spectral index profile along the head–tail source J1331–3141 and radio filament using images at 1070 and 1498 MHz with a common beam of $9\farcs4 \times 8\farcs6$ (Table 1). We used the regions shown in Figure 6(a), i.e., seven regions along the tail (red) and eight regions along the filament (blue). The size of each region was chosen to be larger than at least one beam to sample independent regions. Since the filament is projected onto the radio halo emission that has a spatial surface brightness gradient, we used two large regions on two sides of the filament (black boxes labeled BG1 and BG2) to estimate the background level associated with the diffuse emission from the halo and subtract it from the signal in the regions along the filament. The image does not have sufficient sensitivity to characterize the spatial distribution of the underlying emission, so we simply assumed a linear interpolation between the background regions.

Figure 6(b) shows the spectral index profile along the head–tail source in red. The profile along the filament before the background correction is shown in cyan, and that with background correction is shown in blue. Errors were computed taking into account the local noise level and uncertainty in the background subtraction. The corresponding surface brightnesses at two frequencies in the same regions are shown in Figure 6(c). The emission in the filament has a surface brightness much lower than anywhere in the head–tail source. The background correction to the filament spectral index becomes noticeable in the last region of the filament (F7). Selecting different background regions (i.e., closer to the

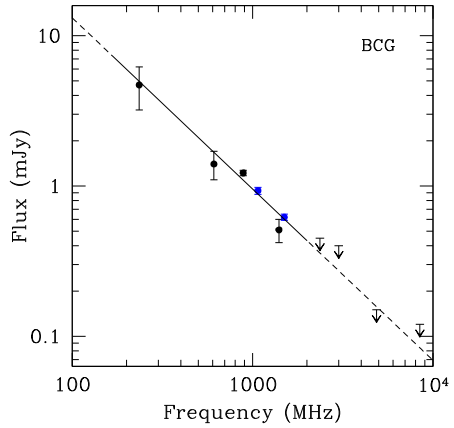

Figure 7. BCG radio spectrum based on the flux densities listed in Table 2. The MeerKAT flux densities, measured on the sub-band images at 1070 and 1498 MHz, are shown in blue. The solid line is the best-fit power-law model with $\alpha_{\rm tot} = -1.1 \pm 0.2$.

southern edge of the filament; the northern background region could not be moved closer because of the fork; see Figure 2(b)) changes the resulting spectral indices by a small fraction of the statistical uncertainties.

The profile along the tail of J1331–3141 is consistent with the head-to-tail steepening already visible in the spectral index image in Figure 4. We fitted the observed spectral steepening using a Jaffe–Perola (JP) model (Jaffe & Perola 1973), in which the timescale for continuous isotropization of the electrons is assumed to be much shorter than the radiative timescale. We also assumed that the expansion velocity of the source is constant and that the break frequency $\nu_{\rm break}$ is proportional to d^2, where d is the distance from the core (e.g., Parma et al. 2007). The best fit is shown as a solid red line in Figure 6(b). The model gives an injection spectral index of $\alpha_{\rm inj} = 0.72 \pm 0.01$ and $\nu_{\rm break} = 2.08 \pm 0.07$ GHz, in very good agreement with the results of a similar spectral analysis carried out by V03 using images at 2.38 and 8.46 GHz.

While the steepening along the head–tail source is consistent with radiative aging of the relativistic electrons, the spectral index along the radio filament—assuming that it is physically connected to the tail—does not follow the prediction of the JP model. Even though the uncertainties are large, instead of steepening, the filament spectral index remains relatively constant around −1.5, the value seen in the tail at the position where the filament branches out (Figure 6(b)). (As noted in Section 4.1, the region of the filament immediately adjacent to the tail is affected by an image artifact, and the spectral index there is not reliable.)

4.3. Radio Spectrum of the BCG

Using the flux densities in Table 2, we derived the radio spectrum of the BCG (Figure 7). There is some scatter, but overall the spectrum is steep with a single slope of $\alpha_{\rm tot} = -1.1 \pm 0.2$ over the 235–1400 MHz interval (the solid line shows the best-fit power-law model). Current 3σ upper limits at higher frequencies suggest a deviation from a simple power-law behavior, suggesting a possible steepening above ∼2 GHz.

We also measured the MeerKAT in-band spectral index for the whole BCG emission and individual components. For the total emission, we obtained $\alpha_{\rm tot} = -1.2 \pm 0.2$, consistent within the errors with the best-fit slope in Figure 7. For the central compact component, we measured $S_{1070,\rm cc} = 0.55 \pm 0.03$ mJy and $S_{1498,\rm cc} = 0.38 \pm 0.02$ mJy using a Gaussian fit, leaving $S_{1070,\rm ext} = 0.38 \pm 0.02$ mJy and $S_{1498,\rm ext} = 0.24 \pm 0.02$ mJy in extended emission. The resulting in-band spectral indices are both quite steep, $\alpha_{\rm cc} = -1.10 \pm 0.23$ (central component) and $\alpha_{\rm ext} = -1.37 \pm 0.29$ (extended).

5. X-Ray Data Reduction

X-ray Chandra and XMM-Newton images of A3562 have been presented and analyzed in earlier works (e.g., F04; G05; Ghizzardi et al. 2010; V22). In this paper, we reanalyze the Chandra observation to compare the newly detected radio features with the brightness and temperature distributions of the thermal gas in the cluster center. We also use an XMM-Newton image and gas temperature map from V22.

5.1. Chandra

A3562 was observed by Chandra in 2003 (OBSID 4167) with ACIS-I for 20 ks. We reprocessed the Level-1 ACIS event file from the archive using CIAO 4.8, following the procedure described in Vikhlinin et al. (2005) using the Chandra Calibration Database (CALDB) 4.8. Following Markevitch et al. (2003), we excluded time intervals with elevated background, which yielded a clean exposure of 18 ks. To model the detector and sky background, we used the blank-sky data sets from the CALDB appropriate for the date of the observation, normalized using the ratio of the observed to blank-sky count rates in the 9.5–12 keV band. Following Markevitch et al. (2000), we also subtracted the ACIS readout artifact. We obtained images in the 0.5–4 keV and 2–7 keV energy bands to detect unrelated X-ray point sources, which were then masked during the image analysis.

6. X-Ray and Radio Analysis

In the X-ray band, A3562 is known to exhibit a very disturbed atmosphere (e.g., Bardelli et al. 2002; F04). It does not possess a central cool core, but rather a warm core (F04; Cavagnolo et al. 2009), with a specific entropy lower than in the surrounding gas. The core appears to be sloshing in response to the passage of the galaxy group SC 1329–313 (currently southwest of A3562) to the north of the cluster (F04), and a cold front is seen southwest of the center (Ghizzardi et al. 2010).

In Figure 8(a), we overlay the MeerKAT high-resolution image contours on the 0.4–5 keV Chandra image of the cluster central region. Panels (b) and (c) show the same Chandra image and an XMM-Newton image in the 0.5–2.5 keV band (V22). A map of the projected gas temperature from the XMM data is shown in Figure 8(d) (V22). The core X-ray emission is highly asymmetric with respect to the BCG location (black plus sign) and is more extended toward the north, as previously noted by F04. The radio filament is oriented tangentially to the cluster center and follows the isophotes of the X-ray core.

We used the cyan sector marked in the images in Figure 8, which encompasses the best-defined part of the radio filament, to extract radial profiles of the radio and X-ray surface brightness. The sector is centered on the centroid of the large-scale cluster X-ray emission, which is offset from the X-ray peak. It also approximately coincides with the center of curvature of the X-ray edge, and thus our profiles describe it accurately. The profiles are shown in Figure 9. The radio profile (red) was extracted on the high-resolution image in Figure 1(a) and shows a clear brightness

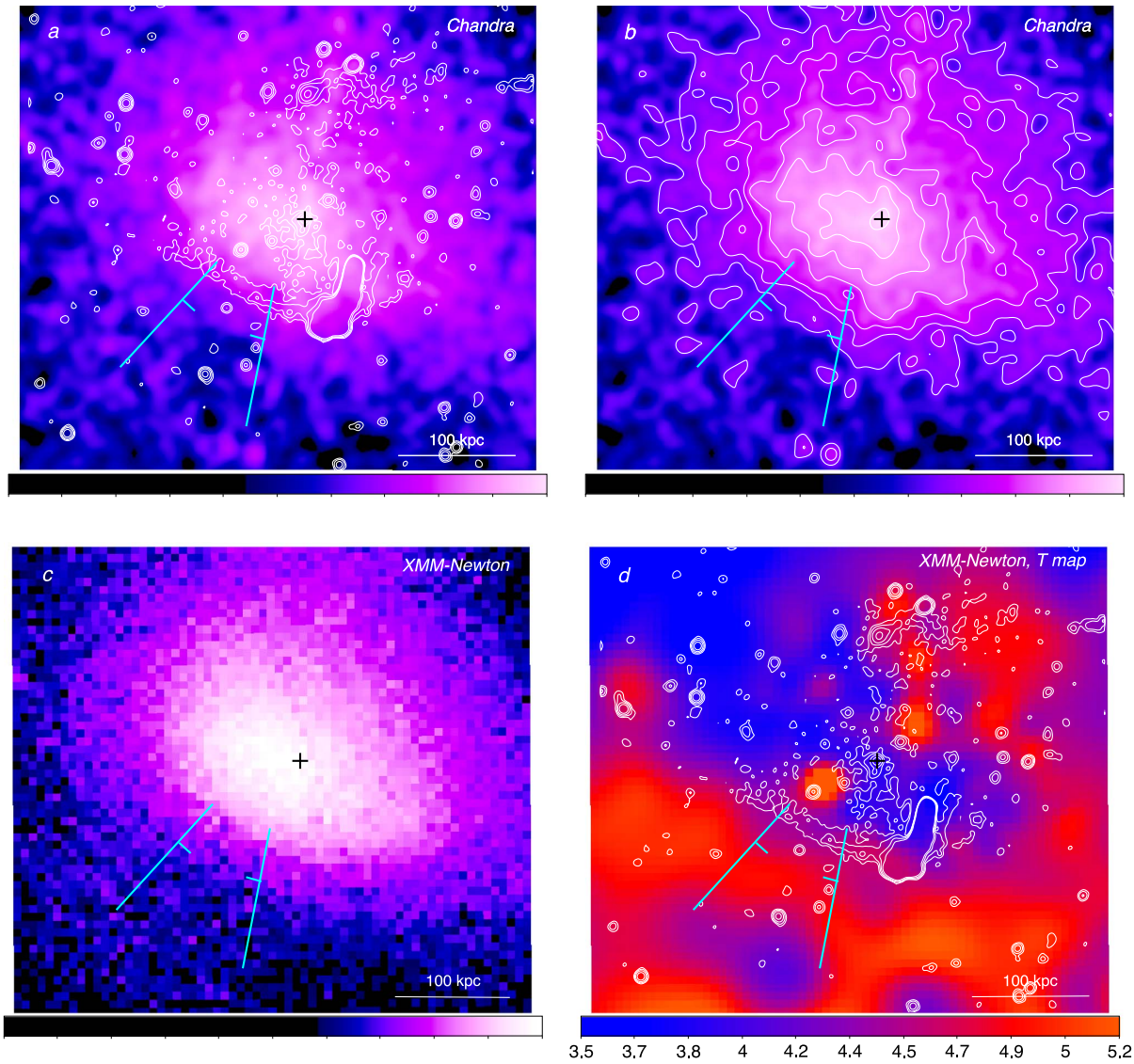

Figure 8. (a) Chandra image in the 0.5–4 keV band, smoothed with a 5″ Gaussian. The image is background subtracted and divided by the exposure map. Radio contours from Figure 1(a) are overlaid at 24 (4σ), 48, 96 and 192 μJy beam^{-1}. (b) Chandra 0.5–4 keV image as in panel (a), with contours of the core X-ray emission overlaid, spaced by a factor of $\sqrt{2}$. (c) XMM-Newton image in the 0.5–2.5 keV band (V22). (d) XMM-Newton temperature map (V22). In all panels, the black plus sign marks the position of the BCG. The cyan sector is used for the radial profiles (Figure 9); short ticks show the position of a cold front. Color bars show the X-ray surface brightness in arbitrary units (panels (a), (b), and (c)) and temperature in keV (panel (d)).

enhancement at the position of the radio filament (red dotted lines). A brightness edge is apparent in the X-ray profiles (marked by the blue dotted line), particularly with Chandra's angular resolution; its position is also marked with cyan ticks in the images in Figure 8. The temperature map in Figure 8(d), as well as a temperature map in F04, shows that the gas inside this edge is cool, so the X-ray edge is a cold front. A similar conclusion was reached based on the radial surface brightness and temperature profiles by Ghizzardi et al. (2010).[20] From the X-ray images, the X-ray edge is much wider than the sector in Figure 8, which we selected to highlight the radio filament. Cold fronts are often seen in cluster sloshing cores, and sloshing is easily set off by any cluster merger as long as there is a negative radial entropy gradient (Markevitch & Vikhlinin 2007), such as we have in A3562 (F04).

The radio filament is parallel to the cold front. However, it is not located at the front but 20″–30″ inward, as seen from the radio brightness profile in Figure 9. The Chandra profile hints at another edge-like X-ray feature (or a bump) at the position of the radio filament. The XMM point-spread function dilutes any sharp features (as indeed seen for the main cold front), but the XMM profile also suggests an inflection at that position, consistent with the presence of another edge (see black dotted line in Figure 9). If this feature is real, it could be a wiggle on the

[20] We note that Ghizzardi et al. (2010) used a different center to extract the X-ray profile (their Figure A.10). The X-ray edge at 100″ from their center ($13^h33^m36\overset{s}{.}8$, $-31^d40'20\overset{''}{.}4$) coincides with the position of the edge in Figure 9 (blue dotted line), at 150″ from our center ($13^h33^m33\overset{s}{.}9$, $-31^d39'51\overset{''}{.}1$).

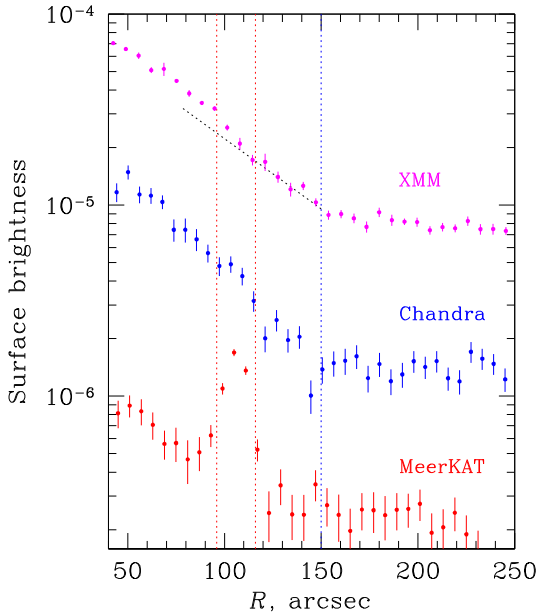

Figure 9. Surface brightness profiles (arbitrary units) for MeerKAT (radio; red), Chandra (X-ray; blue), and XMM-Newton (X-ray; magenta) images, extracted in the sector shown in Figure 8. The radius is from the cluster X-ray centroid. The blue dotted line shows the position of the X-ray cold front (Ghizzardi et al. 2010). Red dotted lines show the radio filament. A hint of a corresponding X-ray front feature is suggested inside the main cold front, though its significance is low. The XMM profile suggests a break at that position consistent with an additional edge (see the black dotted line that matches the profile between the X-ray cold front and the outer edge of the filament).

surface of the cold front seen in projection, or a secondary density edge inside the main front. It may also be a combination of gas *depletion* layers at the location of strong magnetic field filaments (Markevitch & Vikhlinin 2007; ZuHone et al. 2011; Werner et al. 2016a). The possibility that this X-ray bump is inverse Compton emission from the radio filament does not appear to be plausible, as the much brighter source shows no hint of such X-ray excess. A forthcoming deeper Chandra observation will clarify whether this X-ray feature is indeed associated with the radio filament.

7. Discussion

7.1. Origin of the Radio Filament

The new MeerKAT image has revealed a narrow and faint radio filament departing from the end of the J1331–3141 head–tail source and stretching approximately 200 kpc eastward. While we observe a clear spectral steepening along the head–tail source, indicating aging of the relativistic electrons as they move away from the injection site, the spectral index along the filament is instead relatively uniform around $\alpha \sim -1.5$ (although with large uncertainties), which is the value seen in the tail at the position where the filament branches out. This uniformity of the spectrum is similar to that of the MeerKAT radio threads between the lobes of ESO 137–006 (Ramatsoku et al. 2020) and the LOFAR structures in A1033 (de Gasperin et al. 2017), where they also appear to originate from a head–tail source.

We found that the radio filament is parallel to an X-ray cold front seen ∼100 kpc southwest of the cluster center, but located ∼20–30 kpc behind it (toward the cluster) in projection. Numerical simulations of gas sloshing in cluster cores predict prevalent tangential flow of gas under the sloshing cold fronts (ZuHone et al. 2011). If a parcel of gas, enriched with cosmic-ray particles from the head–tail source, gets under the front, the *wind* there would pick it up and stretch it along the front. The tail region of the radio galaxy is advected by the motions of the surrounding cluster plasma. If it were located in the sloshing core, it would be quickly disrupted by the large bulk flows there (e.g., ZuHone et al. 2021). Because it does not appear to feel the wind, the head–tail source is probably outside the dense core and the front. In 3D, cold fronts are convex structures roughly concentric with the cluster X-ray peak. We suggest that the head–tail source is located just outside the front, but projected onto the inside region, with its tail touching the front surface and dipping into a tangential stream of gas under the front, as shown in Figure 10. While the region inside the cold front should be isolated thermally and magnetically from the gas outside the front by draping of the field, it is not perfect, and some field lines cross the front (ZuHone et al. 2013b). The base of the radio filament may be at such a location, where the cosmic-ray electrons from the tail may have diffused under the cold front along such stray lines.

In this picture, the uniformity of the spectral index along the radio filament is explained naturally because all locations along the filament have the same relative radiative age—the parcel of gas of the same initial age is stretched fast by the flow, as opposed to fresh electrons being fed to one end of the tube and slowly traveling along the tube as they age, as in the head–tail source. A problem with this picture is the length of the filament (∼100 kpc for the interval where the spectral index can be measured) and the speed of the wind (∼500 km s^{-1} for a Mach $M = 0.5$ flow), which give the timescale for stretching of ∼200 Myr. During such time, the electrons would (uniformly) age out of the MeerKAT radio band. Thus, reacceleration of the electrons in the filament may be needed. Reacceleration of aged electrons (originating from the head–tail source) by turbulence has been suggested for the A1033 filaments (de Gasperin et al. 2017) that have been named GReET (gently reenergized tail). A very gentle reenergization process is in fact required to explain the brightness and spectral properties of these filaments with $\alpha \approx -4$, in which the particle reacceleration timescale is comparable to the radiative loss timescale of the electrons emitting at LOFAR frequencies. Other cluster radio tails, showing a low-frequency brightness and spectral behavior that is inconsistent with aging models, may be further examples of this gentle reenergization mechanism at work (Cuciti et al. 2018; Wilber et al. 2018; Botteon et al. 2021; Ignesti et al. 2021; Müller et al. 2021). However, this process may not be sufficient to sustain the radio emission seen at GHz frequencies from the A3562 filament, whose radio spectrum ($\alpha \sim -1.5$) is much flatter than, for instance, in A1033.

Alternatively, we may have a much faster stretching. The same tangential flow inside the cold front also stretches and amplifies the normally tangled magnetic field into filaments parallel to the cold front (ZuHone et al. 2011). If the relativistic electrons from the same patch of the tail that dipped into the flow could diffuse along the field lines (rather than simply being advected by the flow) much faster than the Alfvén speed (typically $\lesssim$100 km s^{-1}, probably higher in the amplified field under the cold front) and faster than the gas flow (∼500 km s^{-1}), it may solve the aging problem. However, there is still

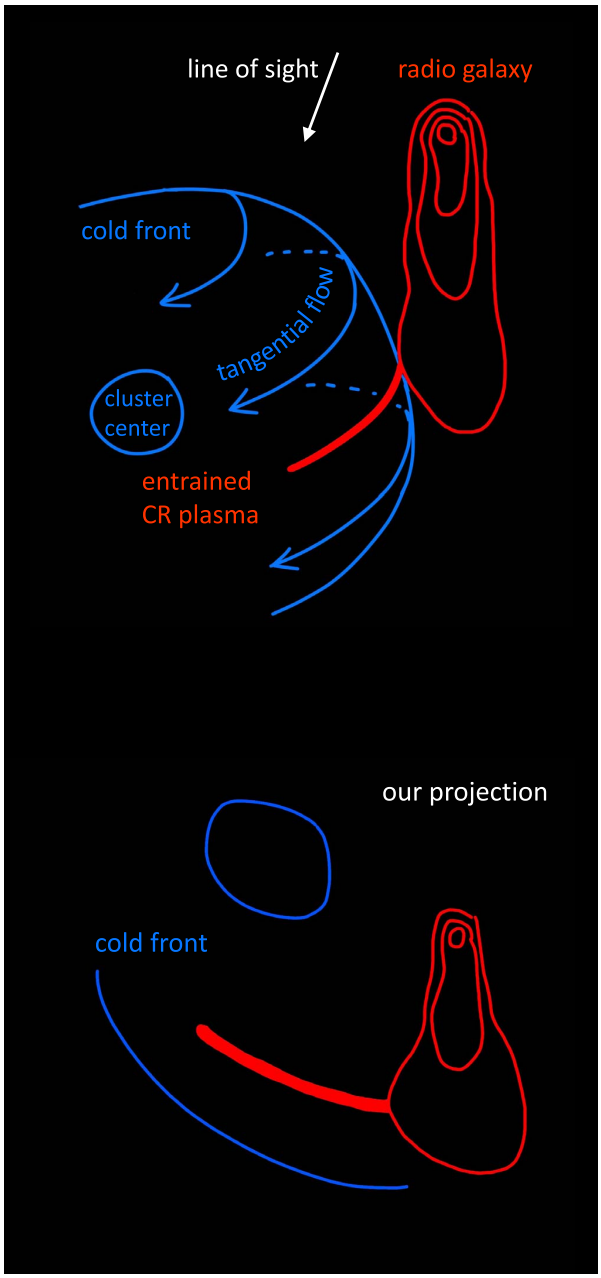

Figure 10. A possible geometry where the radio galaxy is located outside the cold front but dips its tail under the front. The tangential wind under the front entrains a parcel of the cosmic-ray-enriched gas from the tail and stretches it along the flow lines (alternatively, the cosmic-ray electrons diffuse along the magnetic field lines stretched by the gas flow). The bottom panel shows our image plane.

theoretical debate about how fast the cosmic rays can diffuse in the ICM (e.g., Enßlin et al. 2011; Wiener et al. 2013, 2018).

The filament delineates the southern edge of the brighter region of the radio halo that fills the cluster core, and it is interesting to compare it with other examples of such a spatial coincidence. There have been observations of long radio relics located at the edges of giant radio halos, or sharp edges in the radio halo emission, some of which coincide with a shock front seen in the X-ray (e.g., the relic at the edge of the halo in A521, Giacintucci et al. 2008; Brunetti et al. 2008; Bourdin et al. 2013; that in A754, Macario et al. 2011; the radio halo edges in the Bullet Cluster, A520, and Coma Cluster, Markevitch et al. 2005; Vacca et al. 2014; Shimwell et al. 2014; Wang et al. 2018; Hoang et al. 2019; Brown & Rudnick 2011; Bonafede et al. 2022; see van Weeren et al. 2019 for other examples). The physical interpretation there is the shock passage reenergizing the fossil relativistic electrons and igniting a relic, and the same gas inflow that produces the shock front also producing turbulence downstream from the shock (toward the cluster center), which in turn reaccelerates the cosmic-ray electrons that emit the radio halo. In principle, it is possible that the filament in A3562 is a relic on top of a shock at the edge of the halo. However, in the X-ray, we observe a cold front near and parallel to the filament, rather than a shock front. So such a scenario is unlikely, unless the subtle second X-ray brightness edge suggested at the location of the filament (Figure 9) is in fact a shock front outside the core seen in projection onto the core. That edge and the radio filament appear to be very closely concentric with the main cold front (marked by ticks in Figure 8), which would have to be a complete coincidence, and the 3D geometry of the shock would have to be very unlikely (merger shock fronts in clusters tend to propagate in the radial direction, while this one would have to propagate tangentially). Our forthcoming longer X-ray observation with Chandra will clarify the nature (and confirm the existence) of that second X-ray edge. Given the existing data, our interpretation for the filament to arise from stretching by the gas flow under the cold front is more plausible.

Future spectral and polarization radio studies will help us to understand the nature of the filament and potentially provide constraints on the physics of the ICM. In particular, sensitive and high-resolution radio observations of A3562 at lower frequencies (e.g., with the uGMRT) are needed to reduce the uncertainties on the spectral index along the radio filament. Polarization observations will be crucial to estimate the magnetic field strength and structure. Unique to the relics at the shock fronts, there is a steepening of the radio spectrum observed across the relic, from the front downstream (e.g., Giacintucci et al. 2008; van Weeren et al. 2019). If such transverse steepening is observed in the A3562 filament, this would strongly argue for a shock scenario rather than our preferred explanation. This test would require high-sensitivity observations with a higher angular resolution than currently available.

7.2. Origin of the Radio Halo

As discussed above, the radio filament may not mark the location of a shock front, but it may still be connected to the radio halo. V03 suggested that the head–tail radio source may supply the cosmic-ray electrons that feed the radio halo, where they are then reaccelerated, e.g., by turbulence, to counterbalance the synchrotron and inverse Compton energy losses. The newly discovered radio filament may be showing us how the seed cosmic-ray electrons are channeled from the head–tail source into the cluster core. The magnetic field structure inside the cold front is interconnected (and largely isolated from that outside the front; ZuHone et al. 2013b). The electrons from the filament can diffuse throughout the gas inside the front along those connected lines. The radio tail may have provided more seed electrons to the cluster core than those channeled through

this filament. It is possible that there are (or were) other such magnetic crossings of the cold front between the tail and the inner gas, perhaps not always resulting in such highly visible filaments. The turbulence needed to reaccelerate electrons within the core can be produced by sloshing in response to SC group passage (G05), as suggested for radio minihalos by ZuHone et al. (2013a). In the latter work, the seed electrons were proposed to come from disrupted radio lobes of the central radio galaxy; those seeds could be supplied by an external radio galaxy as well (see also Gendron-Marsolais et al. 2021; Biava et al. 2021).

7.3. Southern Radio Extension

We find very faint diffuse radio emission outside the brighter part of the radio halo, in particular, southwest of the core, outside of the radio filament and the cold front ("south emission" in Figure 1(b)). It appears related to the X-ray cluster structure as well—F04 noticed an azimuthally asymmetric enhancement of the X-ray brightness and pseudo-pressure in that region southeast of center just outside the cold front (see their Figures 3 and 5). A similar association (at least in projection) with a higher pseudo-pressure region was reported by G05 for the western extension (Figure 1(b)), which we now see merging at larger distances into the megaparsec-scale bridge connecting the halo and the SC 1329–313 group (V22). The cluster appears to be full of diffuse radio emission at all linear scales, with the brighter region inside the sloshing core with an abrupt boundary at the radio filament—possibly another example of a multicomponent radio halo with a bright minihalo, or minihalo-like emission, in the sloshing core that coexists with a fainter diffuse component outside the core (e.g., Storm et al. 2015; Venturi et al. 2017; Savini et al. 2018; Riseley et al. 2021; Biava et al. 2021).

7.4. A Radio-quiet BCG

The gigantic BCG of A3562 (Figure 3) hosts a very faint radio source with a radio luminosity of 4×10^{21} W Hz^{-1} (Section 3.3) only, namely, 2–3 orders of magnitude lower than cD galaxies with AGNs in clusters of a similar mass (e.g., Hogan et al. 2015). The cD galaxy in the massive, cool-core cluster Ophiuchus has a similar radio-faint nucleus (Murgia et al. 2010; Werner et al. 2016b; Giacintucci et al. 2020). For Ophiuchus, the possible reason was revealed by a high-resolution Chandra image, which shows small-scale sloshing cold fronts and a 2 kpc offset of the peak of the dense gas from the nucleus (Werner et al. 2016b); the peak of the molecular gas shows a similar offset (Hamer et al. 2012). A possible interpretation of these offsets is that the ongoing gas sloshing has temporarily displaced the densest and coolest gas, interrupting the supply of the accretion fuel for the nucleus and thus weakening its radio activity.

While A3562 does not possess a cool core, it has low-entropy gas in its center (F04) that could provide fuel to the radio source, had it been focused on the BCG nucleus. The BCG radio spectrum is quite steep ($\alpha = -1.1$; Section 4.3), suggesting that the radio source is old and possibly unfed. The XMM image in Figure 11 shows that the gas density peak may in fact be offset from the BCG, likely by the same sloshing motions that have created the cold front southwest of the cluster center. The XMM image may even hint at the presence of another cold front near the BCG (see also Figure 8(c), where a vertical edge is seen at the position of the plus sign), as in Ophiuchus, though the image resolution is not sufficient and there is also a chip artifact. The forthcoming Chandra observation should provide a better picture of the gas around the BCG. This stage in the BCG activity cycle is expected to be transient and extremely rare (Hamer et al. 2012), as only a few cluster AGNs with clear offset gas peaks are known to date.

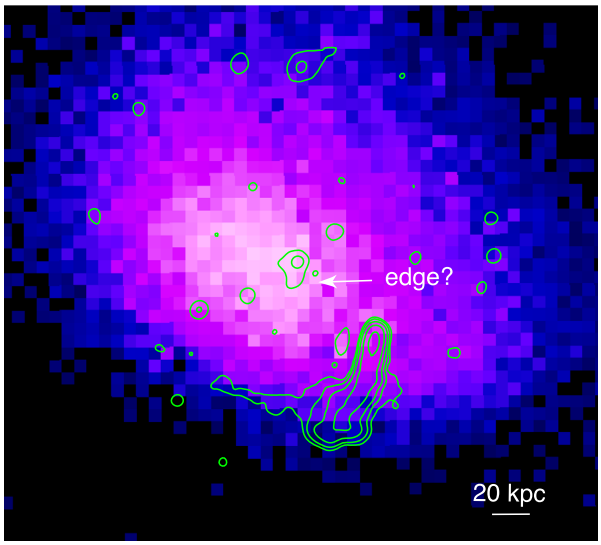

Figure 11. The core of A3562. This is the same XMM X-ray image as in Figure 8(c), with the colors chosen to emphasize the possible X-ray brightness edge near the central galaxy. Radio contours are as in Figure 3.

8. Summary

A MeerKAT observation of the A3562 galaxy cluster revealed a curious narrow, straight synchrotron filament that branches out at a straight angle from the tail of a radio galaxy and spans almost 200 kpc. Its surface brightness is much lower than that of the tail. The radio filament bounds the bright region of the previously known radio halo that fills the cluster. Comparing the radio image with the Chandra and XMM X-ray images, we discover that the filament traces a cold front that delineates the sloshing cluster core—but it stays inside the front in projection.

While the radio galaxy tail shows clear spectral steepening from the head along the tail, the filament shows a rather constant spectral index of $\alpha \simeq -1.5$ (although with large uncertainties). This is also the spectral index of the tail at the distance where the filament is emerging. We speculate that the filament forms where the tail of the radio galaxy, located outside of the sloshing core and the cold front, touches the front. The fast tangential gas flow under the front can stretch the parcel of plasma enriched with cosmic-ray electrons into a narrow filament. It would be natural to have a uniform spectral index along the filament because the age of the electrons is the same along the filament. Some reacceleration is needed in this scenario to maintain the radio filament detectable at the MeerKAT frequencies. Alternatively, we may see anomalously fast diffusion of those electrons from the tail along the magnetic field lines stretched by the gas flow. Our newly discovered synchrotron filament offers an interesting experimental setup to constrain this process.

The radio filament may have been channeling seed electrons from the tail into the region under the cold front, where they are reaccelerated by turbulence and form the radio halo. We also detect radio emission beyond (outside) the filament and the cold front, but its surface brightness is abruptly lower than that inside the filament-bound halo region.

Finally, we detect a faint radio source at the center of the BCG. It is 2–3 orders of magnitude fainter than the typical central BCG in clusters of similar mass. It is likely that the radio source is currently starved of accretion fuel by core sloshing, as seen in a few other clusters such as Ophiuchus.

We thank the referee for their critical and helpful comments. Basic research in radio astronomy at the Naval Research Laboratory is supported by 6.1 Base funding. The MeerKAT telescope is operated by the South African Radio Astronomy Observatory, which is a facility of the National Research Foundation, an agency of the Department of Science and Innovation. The authors acknowledge the contribution of those who designed and built the MeerKAT instrument. The financial assistance of the South African Radio Astronomy Observatory (SARAO) toward this research is hereby acknowledged (www.sarao.ac.za). The Australian SKA Pathfinder is part of the Australia Telescope National Facility, which is managed by CSIRO. Operation of ASKAP is funded by the Australian Government with support from the National Collaborative Research Infrastructure Strategy. ASKAP uses the resources of the Pawsey Supercomputing Centre. Establishment of ASKAP, the Murchison Radio-astronomy Observatory, and the Pawsey Supercomputing Centre are initiatives of the Australian Government, with support from the Government of Western Australia and the Science and Industry Endowment Fund. We acknowledge the Wajarri Yamatji people as the traditional owners of the Observatory site. The National Radio Astronomy Observatory is a facility of the National Science Foundation operated under cooperative agreement by Associated Universities, Inc. The GMRT is run by the National Centre for Radio Astrophysics of the Tata Institute of Fundamental Research. T.V. and G.B. acknowledge the support from the Ministero degli Affari Esteri e della Cooperazione Internazionale, Direzione Generale per la Promozione del Sistema Paese, Progetto di Grande Rilevanza ZA18GR02. H.B. and P.M. acknowledge the financial contribution from the contracts ASI-INAF Athena 2019-27-HH.0, "Attività di Studio per la comunità scientifica di Astrofisica delle Alte Energie e Fisica Astroparticellare" (Accordo Attuativo ASI-INAF No. 2017-14-H.0), from the European Union's Horizon 2020 Programme under the AHEAD2020 project (grant agreement No. 871158), and support from INFN through the InDark initiative. The scientific results reported in this article are based on data obtained from the Chandra Data Archive (ObsID 4167). This research has made use of software provided by the Chandra X-ray Center (CXC) in the application package CIAO.

Appendix
Intercluster Diffuse Radio Emission in the A3562/SC 1319–313 Region

In this appendix, we show a composite MeerKAT/XMM-Newton image of a 2.7 Mpc × 1.5 Mpc region encompassing the galaxy cluster A3562 and nearby galaxy group SC 1329–313 (Figure 12). The X-ray emission is shown as contours. The MeerKAT 1284 MHz image at high resolution (Figure 1(a)) is shown in yellow. In blue, we report the MeerKAT 40″ resolution image of the large-scale diffuse emission obtained by V22 after filtering out the contribution of individual sources. Two megaparsec-scale, faint radio structures, labeled radio arc and radio bridge, are visible in the region between A3562 and SC 1329–313. These structures appear to connect the radio halo in A3562 and diffuse radio source J1332–3146a at the outskirts of the SC group (V22).

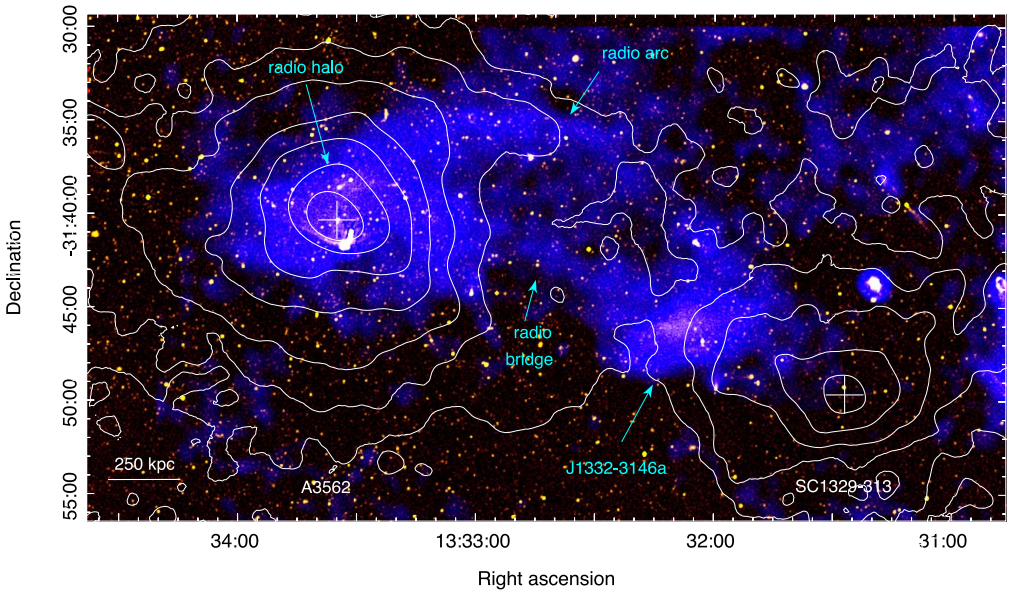

Figure 12. Composite radio/X-ray image of the region of A3562 and nearby galaxy group SC 1329–313. Colors show the MeerKAT image at 6″ resolution (yellow; same as in Figure 1(a)) and the MeerKAT image of the diffuse emission at 40″ resolution (blue; from V22). The XMM-Newton X-ray image in the 0.5–2.5 keV band (V22) is shown as contours, spaced by a factor of 2. White plus signs mark the X-ray centers of A3562 and SC 1329–313.

ORCID iDs

S. Giacintucci https://orcid.org/0000-0002-1634-9886
M. Markevitch https://orcid.org/0000-0003-0144-4052
P. Merluzzi https://orcid.org/0000-0003-3966-2397
S. Bardelli https://orcid.org/0000-0002-8900-0298
O. Smirnov https://orcid.org/0000-0003-1680-7936
G. Bernardi https://orcid.org/0000-0002-0916-7443

References

Bardelli, S., De Grandi, S., Ettori, S., et al. 2002, A&A, 382, 17
Biava, N., de Gasperin, F., Bonafede, A., et al. 2021, MNRAS, 508, 3995
Birkinshaw, M., & Worrall, D. 2015, IAU General Assembly, #29, 2258369
Bonafede, A., Brunetti, G., Rudnick, L., et al. 2022, arXiv:2203.01958
Bonafede, A., Brunetti, G., Vazza, F., et al. 2021, ApJ, 907, 32
Botteon, A., Brunetti, G., van Weeren, R. J., et al. 2020a, ApJ, 897, 93
Botteon, A., Giacintucci, S., Gastaldello, F., et al. 2021, A&A, 649, A37
Botteon, A., van Weeren, R. J., Brunetti, G., et al. 2020b, MNRAS, 499, L11
Bourdin, H., Mazzotta, P., Markevitch, M., et al. 2013, ApJ, 764, 82
Brienza, M., Lovisari, L., Rajpurohit, K., et al. 2022, A&A, 661, 92
Brienza, M., Shimwell, T. W., de Gasperin, F., et al. 2021, NatAs, 5, 1261
Briggs, D. S. 1995, PhDT, New Mexico Institute of Mining and Technology
Brown, S., & Rudnick, L. 2011, MNRAS, 412, 2
Brunetti, G., Giacintucci, S., Cassano, R., et al. 2008, Natur, 455, 944
Brunetti, G., & Jones, T. W. 2014, IJMPD, 23, 1430007
Buta, R. J. 2013, in Planets, Stars and Stellar Systems, ed. T. D. Oswalt & W. C. Keel, Vol. 6 (Dordrecht: Springer Science + Business Media)
Camilo, F., Scholz, P., Serylak, M., et al. 2018, ApJ, 856, 180
Cavagnolo, K. W., Donahue, M., Voit, G. M., & Sun, M. 2009, ApJS, 182, 12
Clarke, A. O., Scaife, A. M. M., Shimwell, T., et al. 2019, A&A, 627, A176
Condon, J. J., Cotton, W. D., White, S. V., et al. 2021, ApJ, 917, 18
Cuciti, V., Brunetti, G., van Weeren, R., et al. 2018, A&A, 609, A61
de Gasperin, F., Intema, H. T., Shimwell, T. W., et al. 2017, SciA, 3, e1701634
Di Gennaro, G., van Weeren, R. J., Hoeft, M., et al. 2018a, ApJ, 865, 24
Di Gennaro, G., Venturi, T., Dallacasa, D., et al. 2018b, A&A, 620, A25
Donnert, J., Vazza, F., Brüggen, M., et al. 2018, SSRv, 214, 122
Enßlin, T., Pfrommer, C., Miniati, F., et al. 2011, A&A, 527, A99
Finoguenov, A., Henriksen, M. J., Briel, U. G., et al. 2004, ApJ, 611, 811
Gendron-Marsolais, M., Hlavacek-Larrondo, J., van Weeren, R. J., et al. 2020, MNRAS, 499, 5791
Gendron-Marsolais, M.-L., Hull, C. L. H., Perley, R., et al. 2021, ApJ, 911, 56
Ghizzardi, S., Rossetti, M., & Molendi, S. 2010, A&A, 516, A32
Giacintucci, S., Markevitch, M., Johnston-Hollitt, M., et al. 2020, ApJ, 891, 1
Giacintucci, S., Venturi, T., Brunetti, G., et al. 2005, A&A, 440, 867
Giacintucci, S., Venturi, T., Macario, G., et al. 2008, A&A, 486, 347
Govoni, F., Orrù, E., Bonafede, A., et al. 2019, Sci, 364, 981
Gupta, Y., Ajithkumar, B., Kale, H. S., et al. 2017, CSci, 113, 707
Haines, C. P., Busarello, G., Merluzzi, P., et al. 2018, MNRAS, 481, 1055
Hamer, S. L., Edge, A. C., Swinbank, A. M., et al. 2012, MNRAS, 421, 3409
Hardcastle, M. J., Croston, J. H., Shimwell, T. W., et al. 2019, MNRAS, 488, 3416
Heywood, I., Camilo, F., Cotton, W. D., et al. 2019, Natur, 573, 235
Heywood, I., Rammala, I., Camilo, F., et al. 2022, ApJ, 925, 165
Hoang, D. N., Shimwell, T. W., van Weeren, R. J., et al. 2019, A&A, 622, A20
Hogan, M. T., Edge, A. C., Hlavacek-Larrondo, J., et al. 2015, MNRAS, 453, 1201
Hotan, A. W., Bunton, J. D., Chippendale, A. P., et al. 2021, PASA, 38, e009
Ignesti, A., Brunetti, G., Shimwell, T., et al. 2022, A&A, 659, 20
Jaffe, W. J., & Perola, G. C. 1973, A&A, 26, 423
Jonas, J. & MeerKAT Team 2016, in Proc. of MeerKAT Science: On the Pathway to the SKA (Trieste: PoS)
Kim, K.-T., Kronberg, P. P., Giovannini, G., et al. 1989, Natur, 341, 720
Knowles, K., Cotton, W. D., Rudnick, L., et al. 2022, A&A, 657, A56
Lacy, M., Baum, S. A., Chandler, C. J., et al. 2020, PASP, 132, 035001
Lane, W. M., Kassim, N. E., Enesslin, T. A., et al. 2002, AJ, 123, 2985
Macario, G., Markevitch, M., Giacintucci, S., et al. 2011, ApJ, 728, 82
Maccagni, F. M., Murgia, M., Serra, P., et al. 2020, A&A, 634, A9
Markevitch, M., Govoni, F., Brunetti, G., et al. 2005, ApJ, 627, 733
Markevitch, M., Mazzotta, P., Vikhlinin, A., et al. 2003, ApJL, 586, L19
Markevitch, M., Ponman, T. J., Nulsen, P. E. J., et al. 2000, ApJ, 541, 542
Markevitch, M., & Vikhlinin, A. 2007, PhR, 443, 1
Mauch, T., Cotton, W. D., Condon, J. J., et al. 2020, ApJ, 888, 61
Merluzzi, P., Busarello, G., Haines, C. P., et al. 2015, MNRAS, 446, 803
Mohan, N., & Rafferty, D. 2015, PyBDSF: Python Blob Detection and Source Finder, Astrophysics Source Code Library, ascl:1502.007
Miller, N. A. 2005, AJ, 130, 2541
Müller, A., Pfrommer, C., Ignesti, A., et al. 2021, MNRAS, 508, 5326
Murgia, M., Eckert, D., Govoni, F., et al. 2010, A&A, 514, A76
Offringa, A. R., McKinley, B., Hurley-Walker, N., et al. 2014, MNRAS, 444, 606
Offringa, A. R., & Smirnov, O. 2017, MNRAS, 471, 301
Owen, F. N., Rudnick, L., Eilek, J., et al. 2014, ApJ, 794, 24
Pandge, M. B., Kale, R., Dabhade, P., et al. 2022, MNRAS, 509, 1837
Parma, P., Murgia, M., de Ruiter, H. R., et al. 2007, A&A, 470, 875
Parrish, I. J., McCourt, M., Quataert, E., et al. 2012, MNRAS, 422, 704
Perley, R. A., Chandler, C. J., Butler, B. J., et al. 2011, ApJL, 739, L1
Quinn, P. J. 1984, ApJ, 279, 596
Rajpurohit, K., Hoeft, M., Vazza, F., et al. 2020, A&A, 636, A30
Ramatsoku, M., Murgia, M., Vacca, V., et al. 2020, A&A, 636, L1
Riseley, C. J., Rajpurohit, K., Loi, F., et al. 2022, MNRAS, 512, 4210
Savini, F., Bonafede, A., Brüggen, M., et al. 2018, MNRAS, 478, 2234
Schweizer, F., & Seitzer, P. 1988, ApJ, 328, 88
Shimwell, T. W., Brown, S., Feain, I. J., et al. 2014, MNRAS, 440, 2901
Shimwell, T. W., Luckin, J., Brüggen, M., et al. 2016, MNRAS, 459, 277
Slee, O. B., Roy, A. L., Murgia, M., et al. 2001, AJ, 122, 1172
Storm, E., Jeltema, T. E., & Rudnick, L. 2015, MNRAS, 448, 2495
Vacca, V., Feretti, L., Giovannini, G., et al. 2014, A&A, 561, A52
van Haarlem, M. P., Wise, M. W., Gunst, A. W., et al. 2013, A&A, 556, A2
van Weeren, R. J., de Gasperin, F., Akamatsu, H., et al. 2019, SSRv, 215, 16
Vazza, F., Wittor, D., Brunetti, G., et al. 2021, A&A, 653, A23
Venturi, T., Bardelli, S., Dallacasa, D., et al. 2003, A&A, 402, 913
Venturi, T., Bardelli, S., Morganti, R., et al. 2000, MNRAS, 314, 594
Venturi, T., Giacintucci, S., Merluzzi, P., et al. 2022, A&A, 660, 81
Venturi, T., Giovannini, G., & Feretti, L. 1990, AJ, 99, 1381
Venturi, T., Rossetti, M., Brunetti, G., et al. 2017, A&A, 603, A125
Vikhlinin, A., Markevitch, M., Murray, S. S., et al. 2005, ApJ, 628, 655
Wang, Q. H. S., Giacintucci, S., & Markevitch, M. 2018, ApJ, 856, 162
Werner, N., ZuHone, J. A., Zhuravleva, I., et al. 2016a, MNRAS, 455, 846
Werner, N., Zhuravleva, I., Canning, R. E. A., et al. 2016b, MNRAS, 460, 2752
Wiener, J., Oh, S. P., & Guo, F. 2013, MNRAS, 434, 2209
Wiener, J., Zweibel, E. G., & Oh, S. P. 2018, MNRAS, 473, 3095
Wilber, A., Brüggen, M., Bonafede, A., et al. 2018, MNRAS, 473, 3536
ZuHone, J. A., Markevitch, M., Brunetti, G., et al. 2013a, ApJ, 762, 78
ZuHone, J. A., Markevitch, M., & Lee, D. 2011, ApJ, 743, 16
ZuHone, J. A., Markevitch, M., Ruszkowski, M., et al. 2013b, ApJ, 762, 69
ZuHone, J. A., Markevitch, M., Weinberger, R., et al. 2021, ApJ, 914, 73